UC Irvine
UC Irvine Electronic Theses and Dissertations

Title
Simulation of Traumatic Brain Injury in Children Using Finite Element Modeling

Permalink
https://escholarship.org/uc/item/5hg1p3gt

Author
Cheng, Ziman

Publication Date
2017

Peer reviewed|Thesis/dissertation

UNIVERSITY OF CALIFORNIA,
IRVINE

Simulation of Traumatic Brain Injury in Children Using Finite Element Modeling

THESIS

submitted in partial satisfaction of the requirements
for the degree of

MASTER OF SCIENCE

in Biomedical Engineering

by

Ziman Cheng

Thesis Committee:
Professor Frithjof Kruggel, Chair
Professor Lydia Su
Associate Professor Gultekin Gulsen

2017

TABLE OF CONTENTS

Page

LIST OF FIGURES

LIST OF TABLES

ACKNOWLEDGEMENTS

I would like to express the deepest gratitude to my committee chair and my supervisor Dr. Frithjof Kruggel for his patient and useful guidance in the past two years. He devoted time and effort in supporting every idea during the completion of this thesis. Also, I would like to express appreciation to my thesis committee members: Dr. Su and Dr. Gulsen for their help and suggestions. Again, special thanks to all my committee members for taking time in this thesis.

Last, I would like to thank my family and friends for being the biggest support of me.

ABSTRACT OF THE THESIS

Simulation of Traumatic Brain Injury in Children Using Finite Element Modeling

By

Ziman Cheng

Master of Engineering in Biomedical Engineering

University of California, Irvine, 2017

Professor Frithjof Kruggel, Chair

Traumatic brain injury is the main cause of disability and death in children and infants. This thesis focuses on establishing the consequences of an external force or impact on brain tissues. FE model has been introduced to investigate the consequences of impact force, either dynamic or static, onto the infant brain. Deformable meshes are involved in FE models to generate time-dependent pressure change in various brain tissues. Results demonstrate that our finite element model is capable of investigating brain tissue pressure transmission within certain impact force and can be used for simulation of minor brain injury in infants.

1   Introduction

1.1   Medical Background

1.1.1   Traumatic brain injury in infants

Traumatic brain injury is the leading cause of disability in children and infants, and sometimes it can even be fatal. The grading criteria for traumatic brain injury is now highly established: mild, moderate, and severe based on the consciousness level or Glasgow coma scale (GCS) score after resuscitation [1]. Patients suffering from mild traumatic brain injury have a considerable chance to fully recover, while short-term memory loss or concentration trouble are still inevitable for most of them. Moderate traumatic brain injury can be lethal. Severe traumatic brain injury patients are of the deeply unconscious, or are not able to follow simple commands. Severe traumatic brain injury bears the risk of death or leading disability in patients, especially in younger people.

Infants and children easily get traumatic brain injury, no matter because of an accident or abusive physical actions. The leading cause of traumatic brain injury in children and infants is falls, followed by vehicle accidents and domestic violence. According to [2], 54.4% of all hospital admissions are due to falls and in 65% of the cases, the head is affected. Falls in children, especially in infants, lead to enormous costs in health care and considerable increase in total lifetime costs.

Almost one third of the fall cases in children, according to emergency department presentations, are resulting in skull fracture. 18% of fall accidents end up in sprains and strains, while open wounds accounts for 17%. Infants that are less than 1 year old are more easily to have head/face injuries (62% of possibility among all the body regions). Young

children (1 to 4 years old) also show the same tendency while the possibility of head/face injury decreases (51%) [3]. Fall simulations are critical in studying traumatic brain injury in children and infants.

The connective tissue absorbs impact force that leads traumatic brain injury. When the impact force exceeds the mechanical limits of brain tissues, moderate or severe traumatic brain injury may occur and inevitably lead to neurological damage [4]. Previous research has demonstrated that neurological injuries do not necessarily occur instantly when fall impacts appear. Rather, they may develop over a period of hours or days [1]. Neurological injuries that occur immediately are called primary injuries. Secondary injury is the term for neurological injuries that developed over time, such as edema. Notably, secondary injury is the major cause of lethal traumatic brain injury. Brain swelling is the typical manifestation of a secondary injury in a child's brain. The occurrence of brain swelling is accompanied by an increase of intracranial pressure that subsequently leads to cerebral perfusion decrease, such as ischaemia [1]. The threshold of systemic blood pressure will decrease subsequently. Intracranial pressure increase, cerebral blood flow reduction and insufficient oxygenation could add the severity of brain damage. Hypoxaemia and hypotension are caused by secondary brain injury [1]. Most patients have symptoms of hypoxaemia and hypotension when they arrive at the hospital, which greatly increases the possibility of poor outcome. For severe cases of edema, the cerebral aqueduct may be blocked, leading to a blockage of CSF flow. Then, the brain stem is pushed into the foramen magnum, leading to death in patients.

Current studies mainly focus on the therapeutic aspect and the pathological aspect of traumatic brain injury, or on the biomechanical properties of brain and neck after fall impact [5][6][7]. How exactly external forces affect the brain tissues is still incompletely understood. This situation could be explained by a fact that controlled impact experiments in children are not ethical, while the results of scientific experiments on feasible animals cannot be simply extrapolated to real children heads. Hence, a bio-simulation system may be a proper environment to study the biomechanical nature of impacts onto children brains. For the simulation, our model is based on arbitrary impact positions and forces could be specified by user. The anatomical information is provided by MR images while biomechanical brain tissue properties are collected from literature reviews.

1.1.2   Brain structures

A key step for the setup of a finite element simulation is given by the compilation of a comprehensive anatomical model.

We divided brain tissues into seven different classes: skull, grey matter, white matter, cerebrospinal fluid, meninges, muscles, and skin. Grey matter, white matter, cerebrospinal fluid and meninges are inside the skull, while muscles and skin, denoted as connective tissue, are outside the skull. Intracranial tissues are more important regarding to traumatic brain injuries since neurological damages occur mainly inside the skull.

The scalp has a thickness of 5 to 7mm, completely covering the skull. The scalp, refers to connective tissue, consists of three layers: the cutaneous layer (hair-bearing skin), the subcutaneous connective-tissue layer, and the muscle and fascial layer [8]. The skull attached to the scalp can be regarded as the most complex structure in the skeletal system

[8]. Brain tissues, eyes, ears, nose, and teeth fit in this bone network neatly. Skull thickness ranges from 4 to 7mm. Scalp and skull protects intracranial tissues due to their thickness and stiffness [8].

Meninges surrounding the brain protect and support brain tissues and the spinal cord. The outer layer is a tough fibrous membrane called dura mater. The inner layer is soft, consisting of two sheets, the arachnoid mater and the pia mater [8]. The brain and the spinal cord are isolated from the body by meninges. Blood vessel networks and nerve sheaths are also part of the meninges so that blood flow and neuronal activities exist. Folds of the meningeal layer constitute the falx cerebri, suspended vertically between the two cerebral hemispheres. The tentorium cerebelli formed by meninges is a shelf on which the posterior cerebral hemispheres are supported [8].
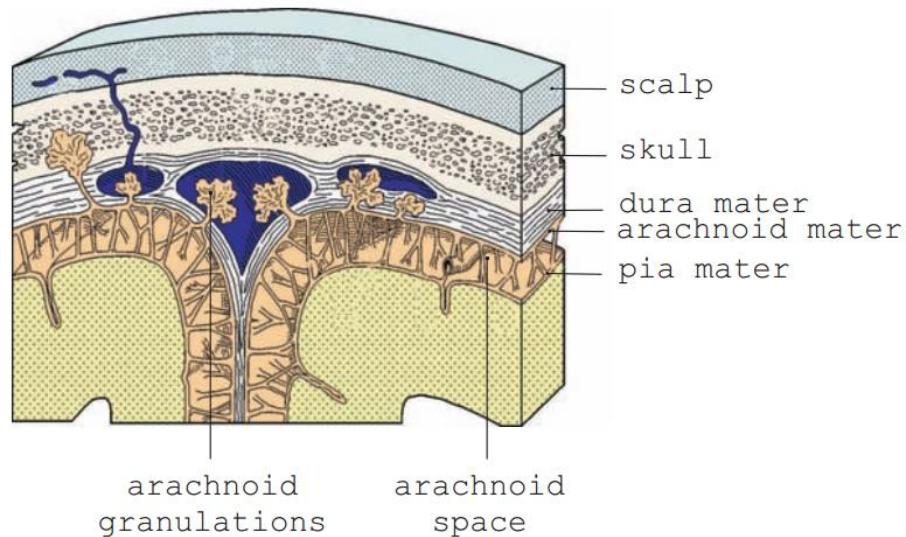

Figure 1: The meninges and cerebrospinal fluid scheme, obtained from [8].

Cerebrospinal fluid (CSF) runs in the subarachnoid space, separating the arachnoid from pia mater. CSF is regarded as the cushion or buffer for the brain when impact appears.

4

The choroid plexus generates the cerebrospinal fluid [8]. CSF flows from the lateral ventricle to the third ventricle and then to the forth ventricle through the aqueduct. Normally, the increase or decrease in CSF volume leads to expansion or shrinkage in brain, stabilizing the brain.

The brain can be divided into five regions anatomically and functionally: cerebrum, cerebellum, midbrain, pons, and medulla oblongata [9]. In this thesis, we mainly discuss the cerebrum. The cerebrum consists of the right and left hemisphere. Left and right hemisphere are divided by the deep fissures into 4 lobes: the frontal lobe, the parietal lobe, the occipital lobe, and the temporal lobe. The outer layer of the cerebrum, the cerebral cortex, is composed of gray matter that contains over 50 billion neurons and 250 billion glial cells called neuroglia. The thicker inner layer is the white matter where interconnecting groups of axons project from the cortex to other cortical areas or from the thalamus (part of diencephalon) to the cortex [8]. To increase the size of the cerebral cortex, the outer convexity of the hemisphere is folded into fissures (sulcus) and folds (gyrus).

1.1.3 Biomechanical properties of brain tissues

Finite element modeling of brain tissue is a demanding task in which are adequate and valid material database is necessary to obtain realistic results. Therefore, gathering accurate and sufficient data on biomechanical characteristics of brain tissues plays an important role for providing the basis for this bio-simulation project.

From previous studies, brain biomechanical properties are often considered as having the stress-strain behavior of filled elastomers [10]. Ogden's theory assumes that the

material mechanical behavior can be described by a strain energy density function. The

stress/strain relationships can be derived from it. Ogden's theory treats brain tissues as

nonlinear elastic materials such as rubber [8]. Miller and Chinzei also have applied

elasticity models to brain tissues for modeling the loading response [8]. However, Ogden's

theory fits both the loading and the unloading response separately, indicating that brain

tissue models can be built by applying pseudo-elasticity. This kind of stress-strain behavior

brought by Ogden's theory can be validated by the uniaxial cyclic tension/compression

experiments on brain tissues conducted by [8] as shown in Fig. 2, in which the empty circle

denotes experiment data and the black curve for Ogden's theory curve. α_i and μ_i are

constitutive parameters calculated from Eq. 1.1, which describes the relationship between

the nominal stress t and the longitudinal stretch.

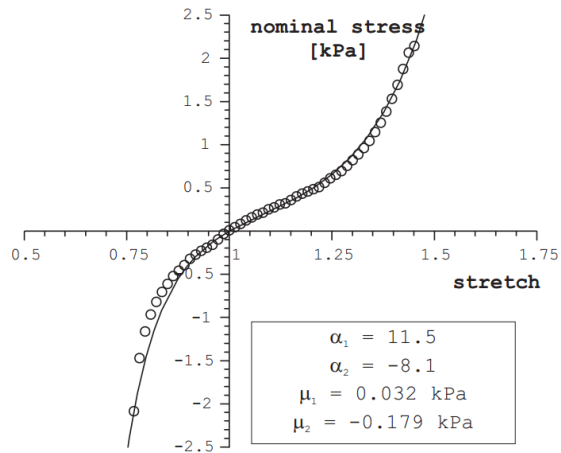$$t = \sum_{i=1}^{N} \mu_i(\lambda^{\alpha_i-1} - \lambda^{-0.5\alpha_i-1}) \tag{1.1}$$

Figure 2: Ogden theory of elasticity, obtained from [8]

Taking energy of brain tissue into consideration is another train of thought

proposed by Ogden and Roxburgh in 1999 [11], dictating the brain material response for

uniaxial stress in terms of pseudo energy function Eq. 1.2. Rubberlike materials have a stress softening phenomenon, called the Mullins effect [8]. The damage function $\phi(\eta)$ from Mullins effect is added in to the strain energy function $w(\lambda)$ corresponding to Ogden's theory. λ stands for the stretch and η is the damage parameter.

$$w(\lambda, \eta) = \eta w(\lambda) + \phi(\eta) \tag{1.2}$$

As shown in Fig. 3, the Mullins effect describes the phenomenon of a rubber specimen which reloads again after a loading and unloading cycle. The Mullins effect also leads to the change on mechanical properties of tissue after a force loading cycle. At a microscopic level, the stress softening phenomenon is often explained as the break of links connecting the filler elastomers and the molecular chains [8].

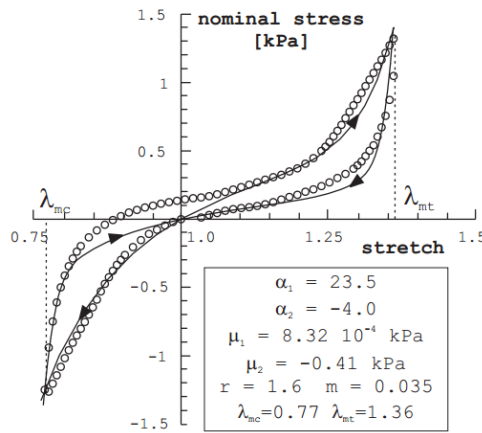*Figure 3: the Mullins effect, obtained from [8]*

Of course, the theory stated above is insufficient for describing biomechanical properties of brain tissues since brain tissues cannot be simply depicted as rubberlike materials nor elastomers. The biomechanical properties of brain tissues are complex. For instance, cartilages in the nasal cavity have fluid-saturated pore. The uniaxial strain/stress

experiments permitting free drainage conducted by [8] provides evidence that consolidate

phenomena exist in brain tissues. This phenomenon has a strong size effect and the

consolidation coefficient is relevant to tissue properties.

Elastic materials are the most common material used in finite element modeling. In

this thesis, we model brain tissues as linear elastic materials. We plan to study other

material properties later in FE models to simulate more delicate mechanical behaviors of

tissues.

1.2   MR image processing

In this thesis, finite element meshes are generated from segmented MR images of an

adult brain. MR images provide the necessary anatomical information for mesh generation.

Magnetic resonance imaging is a widely accepted and effective technique in

acquiring anatomical functional information of brain. It is also a noninvasive method since

no ionizing radiation is involved. Besides, MR images can be used for studying longitudinal

brain morphometry during adolescent development [12].

MRI is useful in detecting and characterizing intracerebral hemorrhage in infants

and children. MRI could be used to identify the parenchymal contusions and further

differentiate the shaken baby syndrome from spontaneous subarachnoid hemorrhage. Soft

tissue swelling, which is another significant symptom of traumatic brain injury, also can be

distinguished by MRI [13].

Although MR images contains necessary brain information for the finite element

model, they cannot be used directly in modeling process. Certain image processing steps

need to be conducted before building FE models. In this thesis, processing includes registration, filtering and segmentation.

Registration is used for aligning two images in the same space. Correspondences across cerebral structures in different modalities can be established by MR image registration. Comparing brain data or tissue across subjects, temporal conditions, and scanners becomes viable through registration.

Linear (rigid) registration is commonly used for aligning data acquired in the same subject while nonlinear methods are required for cross-subject modeling. Linear registration determines a geometric transformation, including rotation, translation and scaling. Eq. 1.3 can be used in calculating parameters of transformation [14]. (x', y', z') is the coordinates of pixel in source image and (x, y, z) is the pixel coordinates in transformed image. $m = \{r_x, r_y, r_x, s_x, s_y, s_z, t_x, t_y, t_z, c_x, c_y, c_z\}$ is the translation parameter.

$$
\begin{bmatrix} x' \\ y' \\ z' \\ 1 \end{bmatrix} = \begin{bmatrix} m_{11} & m_{12} & m_{13} & t_x + w_x \\ m_{21} & m_{22} & m_{23} & t_y + w_y \\ m_{31} & m_{32} & m_{33} & t_z + w_z \\ 0 & 0 & 0 & 1 \end{bmatrix} \begin{bmatrix} x \\ y \\ z \\ 1 \end{bmatrix}
\tag{1.3}
$$

where:

$m_{11} = s_x \cos r_y \cos r_z$

$m_{12} = s_y \cos r_y \sin r_z$

$m_{13} = -s_z \sin r_y$

$m_{21} = s_x (\sin r_x \sin r_y \cos r_z - \cos r_x \sin r_z)$

9

$$m_{22} = s_y(\sin r_x \sin r_y \sin r_z + \cos r_x \sin r_z)$$

$$m_{23} = s_z \sin r_x \cos r_y$$

$$m_{31} = s_x(\sin r_x \sin r_z + \cos r_x \sin r_y \cos r_z)$$

$$m_{32} = s_y(\cos r_x \sin r_y \sin r_z - \sin r_x \cos r_z)$$

$$m_{33} = s_z \sin r_x \cos r_y$$

$$w_x = \cos r_y \left(\sin r_z s_y c_y - \cos r_z s_x c_x\right) + \sin r_y s_z c_z$$

$$w_y = \sin r_x \left(\sin r_y \left(- \sin r_z s_y c_y - \cos r_z s_x c_x\right) - \cos r_y s_z c_z\right)$$
$$+ \cos r_x \left(\sin r_z s_x c_x - \cos r_z s_y c_y\right)$$

$$w_z = \cos r_x \left(\sin r_y \left(\sin r_z s_y c_y - \cos r_z s_x c_x\right) - \cos r_y s_z c_z\right)$$
$$- \sin r_x \left(\sin r_z s_x c_x - \cos r_z s_y c_y\right)$$

Registration optimizes the similarities between two images by modifying the parameters of transformation. In this thesis, a multi-resolution algorithm is employed, using a (global) genetic optimizer and a (local) simplex optimizer.

MR segmentation is another crucial step in image processing. The purpose of MR image segmentation is to divide MR images into regions that are semantically significant, homogeneous, and nonoverlapping with similar attributes such as intensity, depth, color, and texture [15]. The output of the segmentation process is a labeled image where regions ideally correspond to tissue types. MR images in this thesis are labeled into different regions by their anatomical structures: white matter, grey matter, cerebrospinal fluid, meninges, skull, skin, muscle, and so on.

Image segmentation is typical performed by classification of voxel-wise intensity. In this thesis, we use adaptive fuzzy c-means (AFCM) in segmentation. Adaptive fuzzy c-means (AFCM)-based methods can be used to reduce noise level and fuzzy membership by admitting the correction of intensity inhomogeneity and contextual constraints [16]. Intensity inhomogeneities throughout the image volume are a consequence of an imperfect scanner adjustment. These inhomogeneities must be corrected for, otherwise they lead to segmentation errors. Inhomogeneities are modeled as a multiplicative bias field acting on the intensities. This bias field is estimated during the iterative segmentation process.

At boundaries or small structures, intensities mix with between classes leading to classification errors. Intensity inhomogeneities throughout the image volume lead to reginal classification errors. Finally, image artifacts also result in classification errors. Hence, manual segmentation is necessary for certain segmentation purposes. Manual correction by an operator here is necessary. Obviously, manual segmentation takes longer time than computer programs. However, it is the most accurate segmentation method since depicting structures in MR images are difficult for image noise and artifacts. Even though various editing tools have been developed through years, manual segmentation is still an intensive and time-consuming process and constraint by the human operator's previous experience and familiarity of the objective images.

After manual correction, MR images are adequate for finite element modeling process.

1.3   Numerical Background

1.3.1   Introduction to FEM

The finite element method (FEM) is a well-established numerical technique for solving partial differential equations. The FEM is a powerful tool for solving large complex problems in engineering. More recently, finite element methods have been used to study brain biomechanics. Biological tissues are composite and show more complicated mechanical properties than fabricated materials. Finite elements allow modeling the behaviors of a wide range of different tissue types.

The basic idea of FEM is to divide a large domain into smaller and simpler elements, called a mesh. Each finite element is considered as homogeneous in terms of its material properties. Elements have a specified geometry (i.e. hexahedral cubes) that are connected at nodes. A specific material type is assigned to each element. Once the finite element model is assembled, so called boundary conditions are applied. For a biomedical solution, certain nodes are considered as fixed (not movable) while in others, mechanical loads (impacts) are applied. The discretized system is described by a large linear equation system that is solved for the unknown quantities at interest, here, the new node positions of the mesh deformed under load. From the deformed mesh, loaded pressure and velocities can be captured and visualized.

1.3.2   Linear elasticity

According to [17], the stress/strains relationship of any materials can be described as:

$$\tau = C\epsilon \tag{1.4}$$

Where C stands for the material matrix, ϵ is strains and τ is stresses. In finite element model, the stress/strain relationship of each element m is described using

$$\tau^{(m)} = C^{(m)}\epsilon^{(m)} \tag{1.5}$$

In our models, head tissues are assumed to be isotropic and its linear elasticity can be depicting by two mechanical parameters Young's modulus E and the Poisson's ratio v. The material matrix of each element can be defined by Eq. 1.6 [17].

$$C = \frac{E(1-v)}{(1+v)(1-2v)}\begin{bmatrix} 1 & \frac{v}{1-v} & 0 & 0 & 0 & 0 \\ \frac{v}{1-v} & 1 & 0 & 0 & 0 & 0 \\ \frac{v}{1-v} & \frac{v}{1-v} & 0 & 0 & 0 & 0 \\ 0 & 0 & 0 & \frac{1-2v}{2(1-v)} & 0 & 0 \\ 0 & 0 & 0 & 0 & \frac{1-2v}{2(1-v)} & 0 \\ 0 & 0 & 0 & 0 & 0 & \frac{1-2v}{2(1-v)} \end{bmatrix} \tag{1.6}$$

Young's modulus and the Poisson's ratio is used to describe elastic materials. Young's modulus is defined by

$$E \equiv \frac{\sigma(\varepsilon)}{\varepsilon} \tag{1.7}$$

where $\sigma(\varepsilon)$ is the tensile stress, ε is the strain. While Poisson's ratio can be defined by

$$v = -\frac{d\varepsilon_{trans}}{d\varepsilon_{axial}} \tag{1.8}$$

where the ε_{trans} is transverse strain, and ε_{axial} is the strain along the stress axial.

1.3.3 Static finite element model

In static finite element analysis, the deformation of the model can be obtained by

$$KU = R \tag{1.9}$$

where K is the stiffness matrix, U is the vector of displacements, and R is the force vector [17]. Finite element methods are used to find the proper solution for U. The derivation of Eq. 1.9 has been stated below.

Each element in the model has a local coordinate (x, y, z), and the displacement of each element m can be defined by

$$u^{(m)}(x,y,z) = H^{(m)}(x,y,z)\,\widehat{U} \tag{1.10}$$

where $u^{(m)}(x,y,z)$ is the displacement of single element m, $H^{(m)}$ is the displacement interpolation matrix, and $\widehat{U}$ is the virtual displacement vector, consisting of three global displacement components $(U_i,\ V_i,\ W_i)$ [17].

If we differentiate Eq. 1.10, then the strain of each element can be obtained by

$$\epsilon^{(m)} = B^{(m)}\widehat{U} \tag{1.11}$$

where $B^{(m)}$ is the strain-displacement matrix.

Static finite element model stays at the equilibrium state, thus the total internal virtual

displacement should be equal to the total external virtual displacement. According to [17],

this equilibrium state can be described by

$$\int_V \bar{\epsilon}\tau dV = \int_V \bar{U}^T f^B dV + \int_{S_f} \bar{U}^{S_f^T} f^{S_f} dS + \sum_i \bar{U}^{i^T} F_i \qquad (1.12)$$

where f^B, f^{S_f}, and F_i are the loads (force/stress). B denotes the body and S denotes the

surface of an element. Left side of Eq. 1.12 denotes the total internal displacements, while

the right side of Eq.1.12 is the total external displacements.

Virtual displacements of the model can be represented by the sum of displacement of single

element.

$$\sum_m \int_V \bar{\epsilon}^T \tau dV^{(m)}$$

$$= \sum_m \int_{V^{(m)}} \bar{U}^{(m)^T} f^{B(m)} dV^{(m)} + \sum_m \int_{S_f^{(m)}} \bar{U}^{S_f^{(m)^T}} f^{S_f^{(m)}} dS_f^{(m)} \qquad (1.13)$$

$$+ \sum_i \bar{U}^{i^T} F_i$$

By substituting Eq. 1.13 with Eq. 1.5 and Eq. 1. 10, we can get

$$\bar{\hat{U}}^T \left[\sum_m \int_V B^{(m)^T} C^{(m)} B^{(m)} dV^{(m)} \right] \hat{U}$$

$$= \bar{\hat{U}}^T \left[\sum_m \int_{V^{(m)}} H^{(m)^T} f^{B(m)} dV^{(m)} \right. \tag{1.14}$$

$$\left. + \sum_m \int_{S_f^{(m)}} H^{S_f^{(m)^T}} f^{S_f^{(m)}} dS_f^{(m)} + F \right]$$

Where $H^{S_f^{(m)^T}}$, the surface displacement interpolation matrix, can be transformed from $H^{(m)}$.

The body forces, surface forces and concentrated forces of an element can be obtained.

$$R_B = \sum_m \int_{V^{(m)}} H^{(m)^T} f^{B(m)} dV^{(m)} \tag{1.15}$$

$$R_{Sf} = \sum_m \int_{S_f^{(m)}} H^{S_f^{(m)^T}} f^{S_f^{(m)}} dS_f^{(m)} \tag{1.16}$$

$$R_E = F \tag{1.17}$$

Then, we can get

$$\text{R} = R_B + R_{Sf} + R_E \tag{1.18}$$

From the left side of Eq. 1.14, we can obtain the stiffness matrix.

$$K = \sum_m K^{(m)} = \sum_m \int_V B^{(m)^T} C^{(m)} B^{(m)} dV^{(m)} \tag{1.19}$$

Finally, the static element equation Eq. 1.9 is derived. Eq. 1.9 essentially involves the linear elastic property by introducing $C^{(m)}$. Therefore, the model we used have linear elasticity.

It should be noted that large displacement could destroy the equilibrium state, resulting in model collapse.

1.3.4   Dynamic finite element model

In the dynamic FE model, a time-dependent force $R(t)$ is loaded. According to [17], the dynamic finite element equation becomes

$$M\ddot{U}(t) + D\dot{U}(t) + KU(t) = R(t) \tag{1.20}$$

where the displacement matrix becomes time-dependent. M is the mass matrix, D is the damping matrix. This nonlinear differential equation is solved by iteration in temporal domain. In dynamic FE model, inertia forces become considerable and change the body forces R_B. From [17], the body forces vector R_B is given by

$$R_B = \sum_m \int_{V^{(m)}} B^{(m)^T} \left[f^{B(m)} - \rho^{(m)} H^{(m)} \ddot{U} \right] dV^{(m)} \tag{1.21}$$

where $\rho^{(m)}$ refers to the density of single element. Then, Eq. 1.21 can be simplified as

$$M\ddot{U}(t) + KU(t) = R(t) \tag{1.22}$$

The mass matrix M is

$$M = \sum_m M^{(m)} = \sum_m \int_{V^{(m)}} \rho^{(m)} H^{(m)} H^{(m)^T} dV^{(m)} \tag{1.23}$$

Although damping matrix D is critical in studying FE models under vibration, it is not included in this thesis, thus not discussed here.

Hence, FE models used in this thesis are linear elastic both in dynamic and static simulation. The iterative calculation process is utilized to find the optimized solution for the displacement vector. The displacement vector can be converted into pressure change of finite elements by

$$-\Delta P = \frac{(\tau_{xx} + \tau_{yy} + \tau_{zz})}{3} \tag{1.24}$$

where $\tau_{xx}, \tau_{yy}, and\ \tau_{zz}$ are the stresses in the direction of x, y, $and\ z$. Stresses can be calculated by Eq. 1.4, in which the strain vector is the derivative of the displacement vector.

2   Preprocessing

2.1   MR Image Preprocessing

2.1.1   Registration and segmentation

To build the anatomical model for the finite element model, it is necessary to convert the acquired magnetic resonance images into a labeled images, corresponding to the brain tissues types.

The data set analyzed in this thesis were provided by the Human Connectome Project. The dataset was acquired on a Siemens 3T Skyra MRI scanner with 32-channel phased-array head coil and a customized SC72 gradient strength of 100 mTesla/m [18]. To provide optimal image for the later segmentation process, we use a high-resolution dataset composed of a T1 and T2- weighted image. The T1-weighted image was acquired using an MPRAGE protocol (TR: 2400ms, TE: 2.14ms, TI: 1000ms, Flip angle: 8 deg, FOV: 224mm*224mm, Voxel size: 0.6mm isotropic) and the T2-weighted image using (TR: 3200ms, TE: 565ms, Flip angle: variable, FOV: 224mm*224mm, Voxel size: 0.6mm isotropic). Data were downloaded from the Human Connectome Project website in NIFTI format and converted into Brian format before preprocessing [19].

T1-weighted and T2-weighted images show different characteristics. T1-weighted imaging has a strong signal for fat. In T2-weighted imaging, compartments with fluid tend to be brighter and high fat tissues tend to be darker. T2-weighted imaging can be used in pathology demonstration due to the fact that water content increases in most lesions. This difference in the display can be used to characterize anatomical structures. As shown in Fig.

4, the CSF is significantly brighter in the T2-weighted image (bottom) while the white matter and grey matter are brighter in the T1-weighted image (top).

Figure 4: Comparison between T1 and T2-weighted images

First, we registered the T1 and T2-weighted image by a transformation comprised of rotation and translation. A multi-resolution algorithm is employed, using a (global) genetic optimizer and a (local) simplex optimizer. Normalized mutual information is used as a similarity matrix for the cross-modal problems. By combination of information from the T1-weighted imaging and the T2-weighted imaging, tissue properties are better distinguished in the segmentation process.

We classified MR image data sets are classified into 7 intensity classes, roughly corresponding to gray matter, white matter, cerebrospinal fluid, meninges, skull, skin, and muscle. Output of proposed algorithm consists of a set of 7 images, in which each voxel contains the probability that this voxel belongs to a certain class**.**

2.2   Manual Correction (Segmentation) Based on MR Images

As discussed in Section 1.2, various influences lead to segmentation errors that have to be manually corrected. We use an image editing tool to revise the label obtained from segmentation to ensure that different anatomic structures are labeled accurately.

2.2.1   Manual Correction Process

There are mainly three steps in the manual correction process.

First, we revised the labeling of each voxel by its anatomic structure by comparing the label with the original MR image. The majority of mislabeled pixels on each slice are corrected in this step. Fig. 6 shows the uncorrected image.
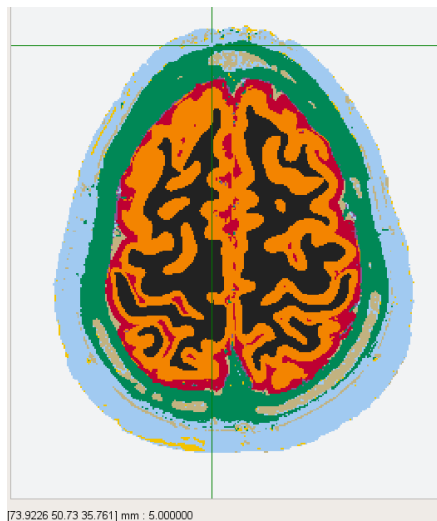

[73.9226 50.73 35.761] mm : 5.000000

Figure 5: MR image before manual segmentation

This step includes the following corrections:

1) The skull: some regions in skull are mislabeled as CSF (grey). Relabel those regions to skull (green).

21

2) The scalp: the scalp (light blue) contains noise and artifacts that needs to be corrected. The small yellow region at the bottom is artifact introduced by scanner. Thin grey line around the skull (green) is mislabeled.

3) The meninges: meninges (purple) can barely be detected in Fig. 6. It should be surrounding the grey matter (red) contiguously. The meninges were added.

4) Other tissue types: minor corrections were conducted. For instance, noise in white matter or grey matter was eliminated pixel by pixel.

Second, we changed voxels in some regions into air. Before the first step, most pixels on one slice are labeled/segmented into a structure/intensity that are relatively close to its desired structure spatially. For example, although there are many ambiguous regions in the boundary intersection of skull and connective tissue, those regions can be easily distinguished and corrected according to their original MR image regions. Some pixels are mislabeled by the segmentation program as the neighboring tissue. For instance, some pixels in the ear canal are labeled as connective tissue at first, while they should be classified as air. Also, the subject of MR images was having a flu during data acquisition process, resulting in fluid-filled nasal cavity. For general study, we changed the fluid into air in nasal cavity. It is relatively easy to correct those pixels by changing the intensity value of these pixels to the background intensity value. Fig. 6 shows a sample of nasal cavity airway. It shows the existence of fluid (green) and air (white) in nasal cavity.
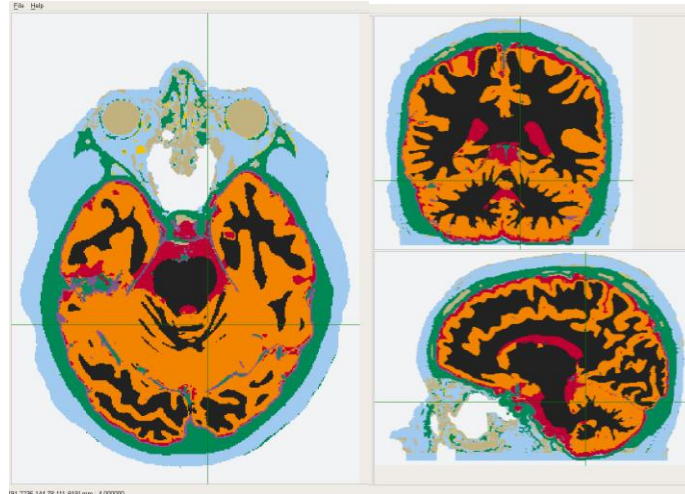
Figure 6: Nasal cavity segmentation

Additionally, two specific structures are missing in the labeled images. (1) The tentorium cerebelli is the dura mater extension separates the cerebellum and the inferior portion of the occipital lobes [20]. (2) The falx is a membrane that separates both cerebral hemisphere. Both structures are crucial when we study the consequences of impact onto the brain, because they separate the intracranial compartment into mechanically decoupled sections. Unfortunately, in most slices, both membranes are thin, and the segmented structure may not be contiguous. Therefore, it is necessary to draw these structures in each slice to reproduce the tentorium cerebelli and falx as accurate as possible. Fig. 7 shows the tentorium structure and the falx structure from sagittal view.
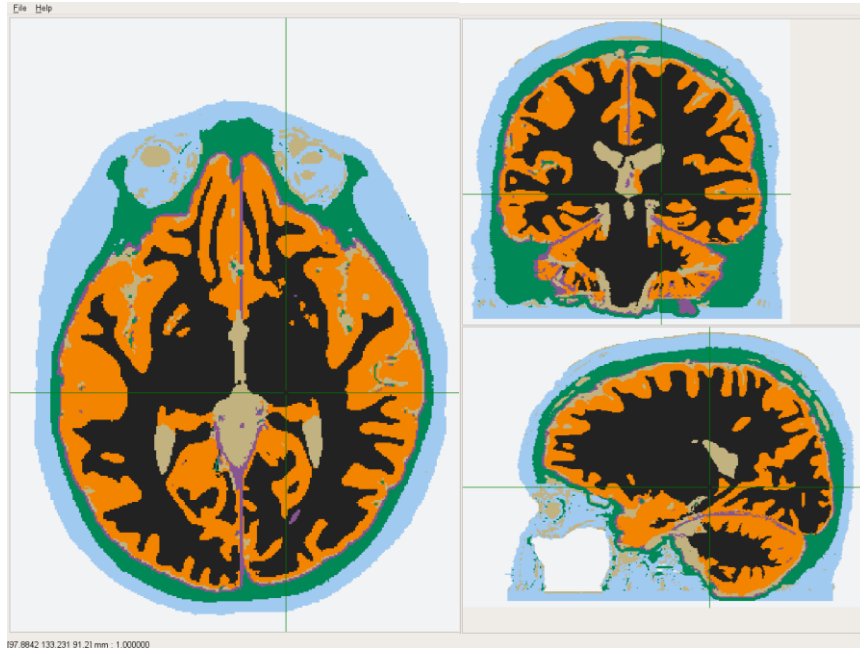
Figure 7: Tentorium structure. Purple line denotes the tentorium structure composed by meninges. Tentorium structure separates cerebrum and cerebellum.

Third, in order to explore the boundary conditions of brain under impact, several slices are added to the bottommost slices at the neck. The neck flexion and extension stiffness is essential for studying the head after impact. In other words, the stiffness of neck constraints over the range of motion in head thereby influences the impact onto the brain. For example, if the neck is fixed or grounded, then the impact force is totally loaded onto the head. In contrast, if the head-neck connection is modeled as springs, then part of the impact force is transferred to the neck and the head can move more freely. According to [5], there is a positive correlation between the stiffness of neck and bending angles. Fig. 8 shows the relationship between head stiffness and angular motions. Because the neck regions were not imaged in the dataset that the last slice of labeled set is chosen and mapped into a slice containing only connective tissues with a region for spinal cord passing

24

through. Slices added mimics the neck with a certain thickness. Later on, this section can be

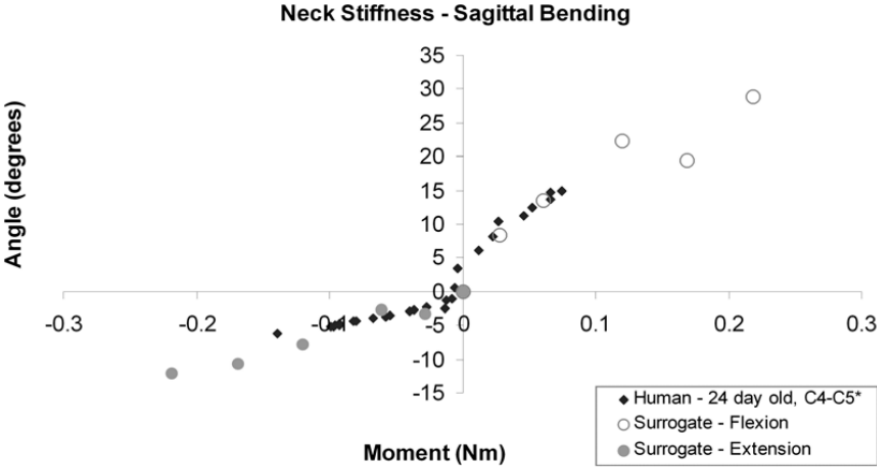modeled with different elasticity to represent different levels of neck flexibility.

Figure 8: Neck stiffness in sagittal bending, obtained from [5].

The outcome of manual correction (segmentation) can be observed in Fig. 7, in

which all seven tissues are segmented and classified into different intensities (colors

representing tissue types).

3   Numerical Methods

3.1   Biomechanical properties of head tissues

As discussed above, we use a linear elastic model due to complexity and time consideration. Biomechanical properties of head tissues we collected from [17]. For finite element modeling, we selected the most consistent information, which are compiled in Table. 1.

Structure	$E[M\,Pa]$	v	$\rho[kg/m^3]$
Scalp(skin, muscle, connective tissues)	16.70	0.42	1200
Skull	6500.00	0.22	1420
White matter	0.12	0.499	1040
Gray matter	0.075	0.499	1040
CSF	0.075	0.49995	1045

Table 1 Brain tissue material biomechanical properties

3.2   Finite Element Modeling

3.2.1   Finite element mesh generation

The labeled image obtained from the preprocessing corresponds to the anatomical model, from which the finite element mesh is generated. Because labeled image is of large scale, we subsample of a labeled image by a factor of 4 into bricks and generate hexahedral cells from the bricks. The subsampling process uses a factor e corresponding to the edge length of bricks. Each cell receives the most common label of the voxels in a brick.

The resulting finite element mesh has a specified resolution of 2.4mm and consists of 225,000 elements and 241,000 nodes.

3.2.2   Finite element model simulations

The FE simulation takes a volumetric mesh and a text file with boundary conditions on input and solves a linear elastic problem on the domain described by the volumetric mesh. The resulting deformed mesh is written into the output file.

Two kinds of simulations using linear elastic models are conducted in this thesis, the static simulation and the dynamic simulation. In the static simulation, a static force has been loaded onto a region on the surface of the brain. In the dynamic simulation, the force is changing in a sinusoidal pattern and, at each time step, a mesh is generated and stored at each time step so that dynamic variation of pressure in brain tissues can be observed.

At each simulation, a mesh with its cells denoting pressure changes is obtained. The pressure variation of brain tissues can be visualized in a set of images converted from mesh. Because pressure variation varies dramatically in different tissues, we also use the logarithms of the pressure variation for visualization.

4   Experiments

4.1   Experimental design

To determine the appropriate impact force setup, we first researched the available medical literature and compiled impact forces for different experiment objectives. Most publications state that medical records are not suitable as sources for experiment settings because report of caregivers are subjective and unreliable. Hence, we tend to use experiment data derived from previous research using surrogates representing infants and young children.

In the laboratory investigation conducted by [5], an infant surrogate had been assembled to evaluate the possibility of brain injury in infants falling from low heights. For infants falling from 0.3m and 0.6m height, the impact force measured is approximately 600N for hitting a soft ground (carpet or mattress), while hitting a concrete ground, no matter from 0.6m or 0.9m height, leads to an impact force of 1000N [5].

In [3], the scientists collected nearly 450 individual medical cases of injuries due to infants or children fall in UK 2015. For severe injury like skull fracture or intracranial injuries, most patients (76.6%) are younger than 12 months and 23.4% of patients are aged between 13 and 48 months. Conversely, infants (younger than 12 months) are less likely to suffer from minor injuries, which occurs more often (76%) in toddlers (13-48 months). Importantly, the most frequent impact region (63.5%) that leads to a fracture or intracranial injury are found for parietal and temporal areas of the skull. Minor head injuries are typically found as consequences of impacts on the forehead (47.1%).

Comprehensively, the experiment is designed in the following two ways.

Static simulation: simulating the consequences of a fall impact onto the brain. The fall height is less than or equal to 0.6m onto a soft ground resulting in minor brain injury in the forehead region.

Dynamic simulation: simulate dynamic changes due to impacts. For instance, skull pressure transmission and the meninges' shield ability for two hemispheres.

The neck is fixed in all simulations.

4.2   Static simulation

In this simulation, the impact force is set to be 10N, 30N, 50N, 100N and 600N respectively. Dataset is collected from former literature [5]. We use a static simulation to calculate the brain tissue pressure variation after the impact force loaded on the forehead.

The impact region was chosen from the mesh generated from subsamples, which is of 2.4mm resolution, derived from the segmented images. Location of cells which have been chosen to interact with impact force is shown in Fig. 9. The green cross denotes the cell used in frontal impact experiments. Coordinates at the right bottom represents the spatial position of the specified cell, which is [79 41 40]. Value outside of square brackets demonstrates equilibrium state of the mesh.
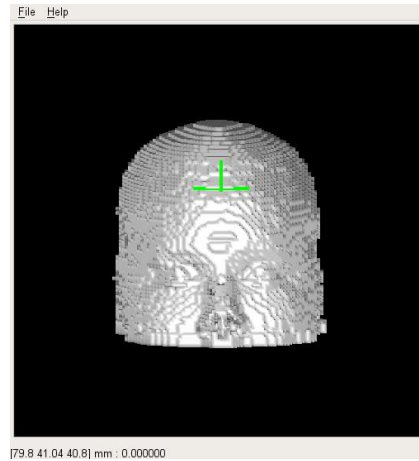
Figure 9:Finite element mesh generated from low resolution subsamples

The mesh after impact force of 10N onto the forehead is shown in Fig. 10, two different colors denote the increased or decreased pressure on each mesh cell and the variant value of each cell is displayed at the left bottom corner. On the forehead, where the impact force was loaded, pressure changes greatly (see Fig. 10). The parietal region also shows an increase in pressure, indicating that impact force was transferring from the forehead to the back of head. Red denotes positive pressure, green denotes negative pressure.
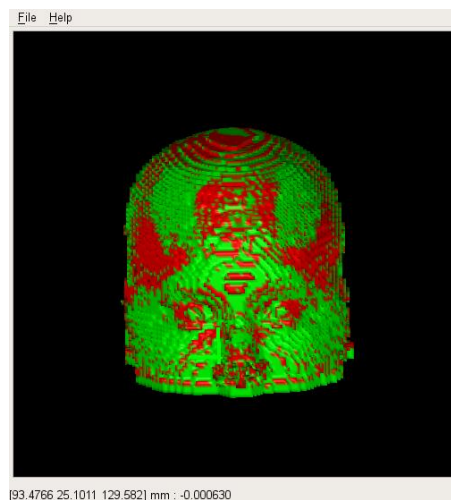

Figure 10: Representation of pressure variance in deformed mesh.

Unfortunately, the impact force set (30N, 50N, 100N and 600N) to be simulate real case fall injury is not suitable in this model, exceeding the mechanical limit of tissues which seem to be "smashed" away from their original position in Fig. 11. The top of left image shows the dynamic deformation of forehead connective tissue and part of skull, which is not suitable for further investigation of brain tissue mechanical variations since the mesh can be regarded as collapsed. Therefore, the following static simulation discussion is based on small impact force (10N).
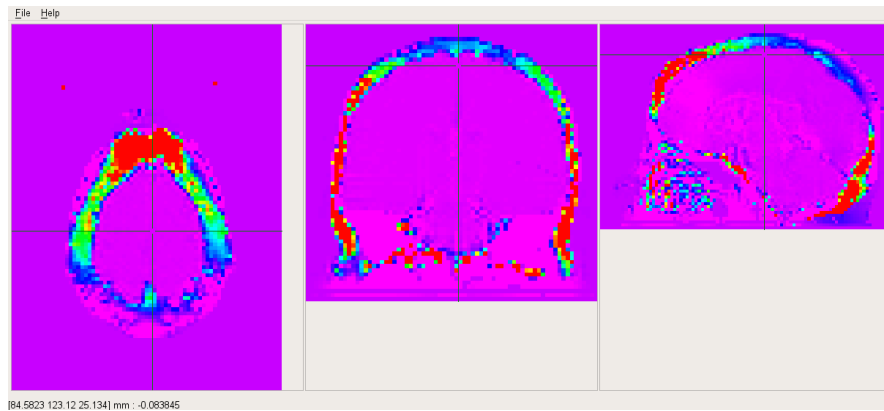

Figure 11:Tissue deformation in forehead after impact.

To better investigate the force transmission in intracranial regions, orthogonal sections of the stress-loaded mesh are shown in Fig. 12. Clearly, the pressure existed on the skull is strongly positive in forehead and parietal area, while the pressure on white matter is nearly zero. We concluded that the skull protects the brain and pressure transfers through skull to minimize the impact on intracranial tissues.
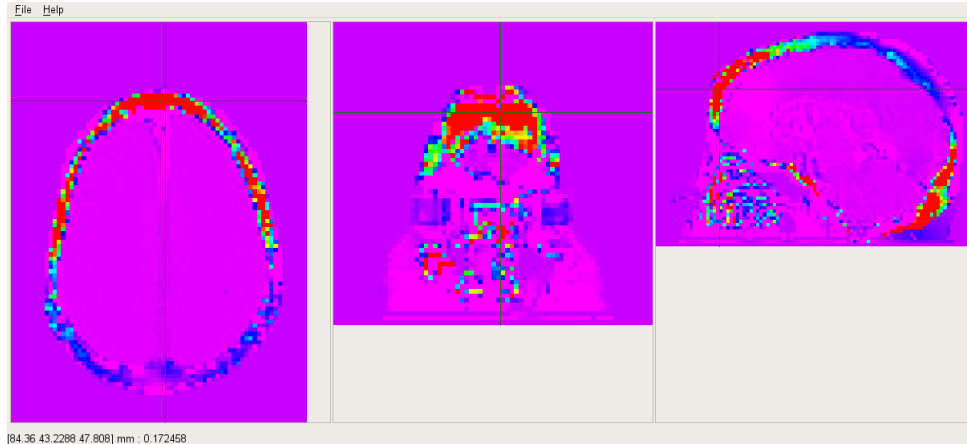
Figure 12: Skull pressure variance after static impact

4.2 Dynamic simulation

4.2.1 Simulation setup

In this simulation, two set of experiments are carried out to test for the ability of FE models in describing brain tissue biomechanical properties. A dynamic simulation introduces mass and inertia effects to the model, that allows a more realistic simulation. Pressure changes in brain tissues can be observed dynamically and presents different material properties more distinctly. We modeled the time-dependent impact force as a sinusoidal curve.

Experiment set one: the impact region is on the forehead with a force of 10N, deriving from prior tests conducted in static simulation. The vector of impact force is perpendicular to the forehead region surface. The impact location is the same as static simulation in Fig. 13 of coordinate [79 41 40]. The purpose is to investigate the actual dynamic process of pressure change on skull happened in the static simulation.

Experiment set two: the impact region is in the temporal region with a force of 10N perpendicular to the right temporal region of infant head, pointing towards the center of

the head. The impact time-period is 20ms with a step size of 0.5ms. The impact location is

shown in Fig. 16 of coordinate [152 118 52]. The objective of this experiment is to

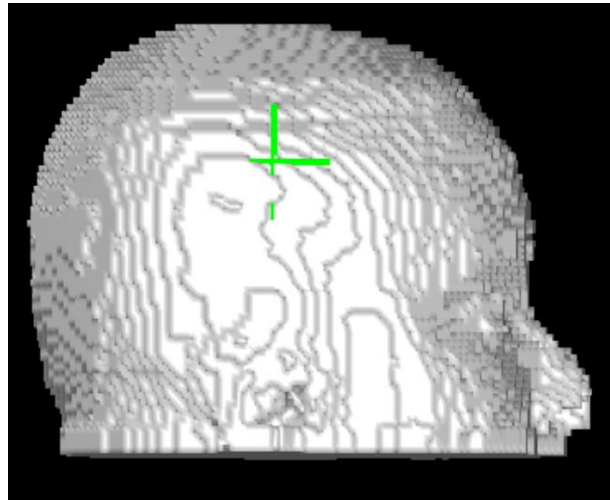demonstrate the shield effect of the meninges in decoupling both hemispheres.

Figure 13: Impact onto the temporal region

4.2.2   Dynamic simulation results

4.2.2.1   Experiment set one

The impact on forehead experiment calculated and stored 40 stress-loaded meshes

at 0.5ms intervals during a 20ms period. Each mesh visualizes the brain tissue pressure at

that specific time point. Throughout all the time steps, the dynamic change of pressure on

different tissues can be investigated. We chose 20 time points of intervals of 1ms to display

the change in pressure in different positions on skull (front, top, back). The coordinates of

the chosen cells are [75 43 46] for the forehead, [75 148 14] for the top, and [75 189 134]

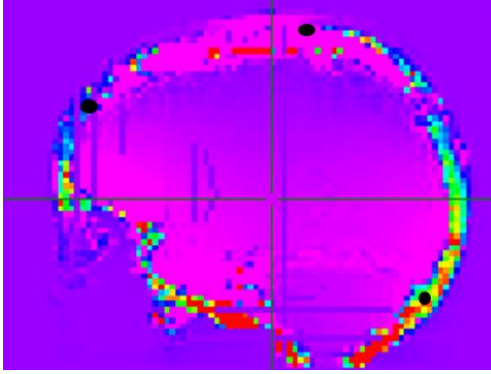for the back as well as the occipital region (see black dots in Fig. 14).

Figure 14: Selection of regions on the skull

The pressure curve of frontal skull and occipital skull positions (Fig. 15) shows the same sinusoidal pattern, while the pressure at the top position does not show much variation. This phenomenon might be described as that the forehead skull transfers pressure to the back skull through ambilateral bone structures, not through the top bone. This assumption is consistent with skull structure which has cracks formed by fontal skulls and left-right temporal skulls. Also, we can observe that the peak pressure on frontal skull and occipital skull are almost appearing simultaneously, which could be explained as the skull pressure transmission are faster than the time step we specified. Besides, the peak pressure at the frontal position is much larger than that at the occipital position, matching the natural assumption that the impact region absorbs the most of impact.
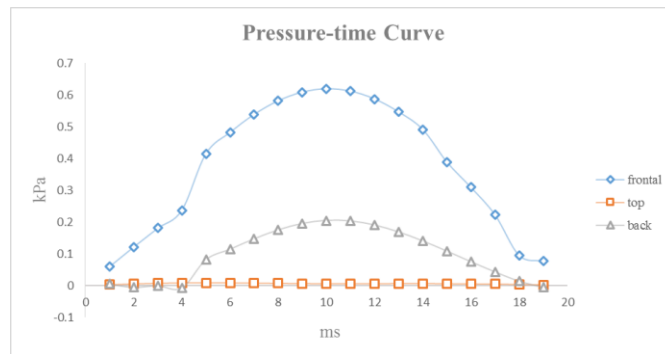

Figure 15: pressure-time curve on three different regions of skull

34

4.2.2.2   Experiment set two

The experiment acquires data from four different time point. Fig. 16 below shows the orthogonal sections through the head at time points, from top to bottom: at 0.5ms, 1.0ms, 1.5ms, 2.0ms. The color scale in three rows are the same, with red corresponding to greater positive pressure, and blue to smaller positive pressure.
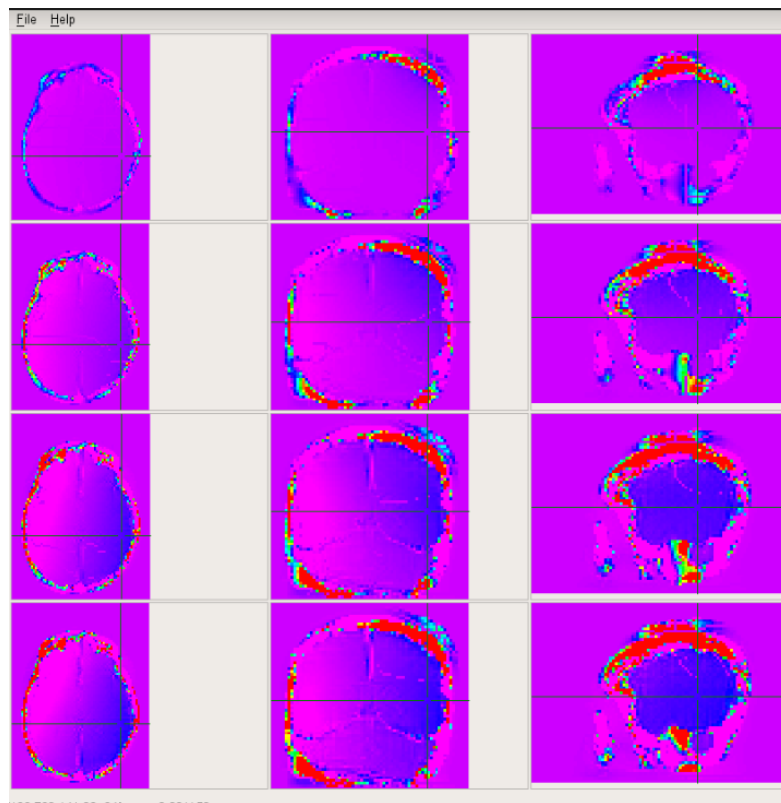

Figure 16: Mesh phase at starting time points.

Remember that the force was loaded on the right side of the head. The pressure on the temporal skull is gradually increase over time, accompanied with pressure increase at right hemisphere. The falx and tentorium structure shows dramatical pressure change across meninges. This may demonstrate that the meninges absorb impact, protecting brain tissues.

Choosing time points in the middle of the period (at 10ms, 10.5ms, 11ms, 11.5ms), we can observe that the pressure in the intracranial region are near zero (see Fig. 17), while the impact force is maximum. Also, the pressure on right temporal skull is greater than other tissues, demonstrating that the skull protects intracranial tissues.
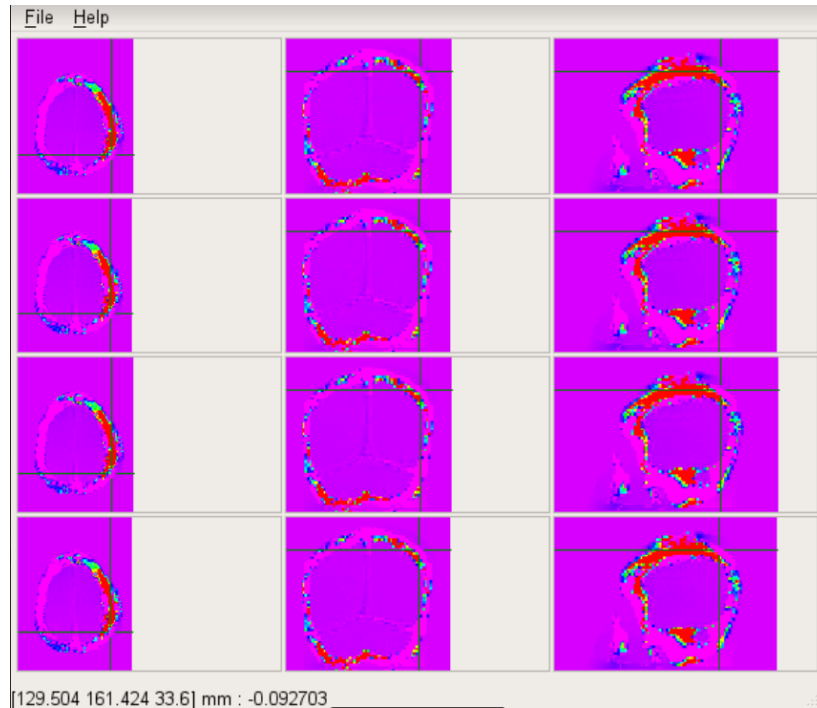

Figure 17: Visualized pressure at middle time points

5   Conclusion and Prospect

The finite element model used in this thesis has proven to be able to simulate impact with small forces onto the brain with small force values (smaller than 30N). We investigated the role of meninges and skull due to impacts. Skull and meninges absorbs impact force and protects the intracranial tissues. Results from dynamic simulations correlate with biological and mechanical properties of brain tissues. Hence, this finite element model is capable of investigating brain tissue pressure transmission within certain impact force and can be used for simulation of minor brain injury in infants. Combing both, the FE model has ethical, effective, and quantitative advantages that can be used replace cadaver experiments and laborious medical record collections.

In this thesis, tissue properties are modeled as linear elastic materials. In fact, almost all the brain tissues have nonlinear mechanical properties. Linear elastic models are not accurate enough to simulate more complex properties of tissues. Due to subsampling used in mesh, some important information is lost. For instance, CSF is almost not represented because it forms just a thin layer between gray matter and the meninges. CSF has an important function as cushion for the brain. The study on CSF should be included in the future research.

In the future, this FE model will include nonlinear elastic material properties with higher resolution to investigate more complicated brain tissue related problems since brain tissues behave nonlinearly and biphasic properties have been observed. More specific medical case should be collected to simulate more realistic accidental injuries. For example, forces and time-period should be collected more accurately to simulate realist fall

in child. A more sophisticated FE model denoting realistic brain tissue interactions should

be developed in the future for higher medical demands and more delicate scientific

purposes.

References

[1] J. Ghajar, "Traumatic brain injury", *The Lancet*, vol. 356, no. 9233, pp. 923-929, 2000.

[2] Y. Miyazaki, M. Mochimaru, Y. Nishida, M. Kouchi and S. Ujihashi, "Visualization of Injury Hazard of a Playground Equipment using Children Fall Simulator", *Journal of the Robotics Society of Japan*, vol. 26, no. 6, pp. 561-567, 2008.

[3] J. Hughes, S. Maguire, M. Jones, P. Theobald and A. Kemp, "Biomechanical characteristics of head injuries from falls in children younger than 48 months", *Archives of Disease in Childhood*, vol. 101, no. 4, pp. 310-315, 2015.

[4] J. Bruns and W. Hauser, "The Epidemiology of Traumatic Brain Injury: A Review", *Epilepsia*, vol. 44, pp. 2-10, 2003.

[5] B. Coats and S. Margulies, "Potential for head injuries in infants from low-height falls", *Journal of Neurosurgery: Pediatrics*, vol. 2, no. 5, pp. 321-330, 2008.

[6] N. Ibrahim and S. Margulies, "Biomechanics of the toddler head during low-height falls: an anthropomorphic dummy analysis", *Journal of Neurosurgery: Pediatrics*, vol. 6, no. 1, pp. 57-68, 2010.

[7] M. Douglas-Escobar and M. Weiss, "Biomarkers of Brain Injury in the Premature Infant", *Frontiers in Neurology*, vol. 3, pp.185-185, 2013.

[8] G. Franceschini, "The mechanics of human brain tissue." *Modelling, preservation and control of materials and structures, University of Trento*, 2006.

[9] W. Penfield, and H. Jasper, "Epilepsy and the functional anatomy of the human brain", Oxford, England, 1995.

[10] SimBio Consortium. "SimBio: A generic environment for bio-numerical simulation", 2000.

[11] R. Ogden, "Non-linear elastic deformations", *Engineering Analysis*, vol. 1, no. 2, p. 119, 1984.

[12] N. Gogtay, J. Giedd, L. Lusk, K. Hayashi, D. Greenstein, A. Vaituzis, T. Nugent, D. Herman, L. Clasen, A. Toga, J. Rapoport and P. Thompson, "Dynamic mapping of human cortical development during childhood through early adulthood", *Proceedings of the National Academy of Sciences*, vol. 101, no. 21, pp. 8174-8179, 2004.

[13] F. Bandak, "Shaken baby syndrome: A biomechanics analysis of injury mechanisms", *Forensic Science International*, vol. 151, no. 1, pp. 71-79, 2005.

[14] G. Tzimiropoulos, V. Argyriou, S. Zafeiriou and T. Stathaki, "Robust FFT-Based Scale-Invariant Image Registration with Image Gradients", *IEEE Transactions on Pattern Analysis and Machine Intelligence*, vol. 32, no. 10, pp. 1899-1906, 2010.

[15] L. Clarke, R. Velthuizen, M. Camacho, J. Heine, M. Vaidyanathan, L. Hall, R. Thatcher and M. Silbiger, "MRI segmentation: Methods and applications", *Magnetic Resonance Imaging*, vol. 13, no. 3, pp. 343-368, 1995.

[16] R. He, S. Datta, B. Sajja and P. Narayana, "Generalized fuzzy clustering for segmentation of multi-spectral magnetic resonance images", *Computerized Medical Imaging and Graphics*, vol. 32, no. 5, pp. 353-366, 2008.

[17] Y. Zhang, "A Bio-Medical Model of the Human Head for Impact Simulation", Thesis, 2015.

[18] E. Kaden, F. Kruggel and D. Alexander, "Quantitative mapping of the per-axon diffusion coefficients in brain white matter", *Magnetic Resonance in Medicine*, vol. 75, no. 4, pp. 1752-1763, 2015.

[19] "Human Connectome Project | Mapping the human brain connectivity", Humanconnectomeproject.org, 2017. [Online]. Available: http://www.humanconnectomeproject.org/. [Accessed: 02- Jun- 2017].

[20] L. Picard, S. Bracard, C. Islak, D. Roy, A. Moreno, J. C. Marchal, and J. Rolan, "Dural fistulae of the tentorium cerebelli. Radioanatomical, clinical and therapeutic considerations." *Journal of neuroradiology. Journal de neuroradiologie,* vol. 17, no. 3, pp. 161-181, 1989.